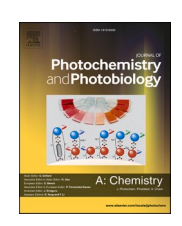


Contents lists available at ScienceDirect

Journal of Photochemistry & Photobiology, A: Chemistry

journal homepage: www.elsevier.com/locate/jphotochem





Hierarchical TiO_2 -g- C_3N_4 photocatalyst with purification effect for NO_x oxidation under cyan light

Ahmed Al Mayyahi ^a, Archana Sekar ^b, Sabari Rajendran ^b, Shusil Sigdel ^c, Lianying Lu ^d, Juan Wang ^d, Guohong Wang ^d, Jun Li ^b, Placidus B. Amama ^{a,*}

- ^a Tim Taylor Department of Chemical Engineering, Kansas State University, Manhattan, KS 66506, USA
- ^b Department of Chemistry, Kansas State University, Manhattan, KS 66506, USA
- ^c Department of Physics, Kansas State University, Manhattan, KS 66506, USA
- ^d College of Chemistry and Chemical Engineering, Hubei Normal University, Huangshi 435002, PR China

ARTICLE INFO

Keywords: Hierarchical TiO₂-g-C₃N₄ NO_x oxidation Relative humidity Recycled photocatalyst Z-Scheme DeNO_x index

ABSTRACT

NO_x photocatalytic oxidation is a promising approach for practical NO_x abatement at sub-ppb levels and under ambient conditions. However, conventional photocatalysts are characterized by their low NO_x adsorption capacity and activity under visible light. This results in poor NO (g) conversion and may form more toxic NO2 (g), hampering the utilization of photocatalysis in NO_x removal. Herein, we employed a hierarchical macromesoporous structure composed of Z-scheme TiO₂-g-C₃N₄ hybrid embedded in parallel TiO₂ channels as a high adsorption capacity and low band gap photocatalyst for NO_x oxidation. This unique structure provides aligned macroporous channels and mesoporous walls for efficient NO_x adsorption and storage of NO_x oxidation product (i.e., NO_3 (s)) while enabling visible light absorption. NO_x oxidation was conducted in a laminar-flow reactor under 50% relative humidity and simultaneous exposure to blue and green lights (cyan light). TiO2-g-C₃N₄ showed NO conversion (37%) which is four times higher than that of TiO₂ (7%) and two times higher than that of g- G_3N_4 (17%). In addition, TiO_2 -g- G_3N_4 hybrids showed high NO_x adsorption capacity and converted NO_x to nontoxic NO_3^- with minimal formation of NO_2 , evident by its positive $DeNO_x$ index (+74 ppm) in contrast to g- C_3N_4 with a negative DeNO_x (-4 ppm) and TiO₂ with a slightly positive DeNO_x index (+15 ppm). The study demonstrates the delicate relationship between H_2O adsorption on the hybrid structure and NO_x photooxidation reaction and provides detailed mechanistic insights on the photocatalytic response. It is expected that the results of this study will benefit ongoing efforts to design visible-light active photocatalysts.

1. Introduction

Air pollution is a considerable environmental threat that is not only associated with climate change but also linked to the deaths of 100000-200000 individuals per year in the United States [1–4]. Nitrogen oxides (NO_x) are among the most serious air pollutants that impact human respiratory systems and serve as precursors for ozone and haze formation [5,6]. A significant portion of NO_x is generated anthropogenically by high-temperature processes involving the presence of nitrogen and oxygen, such as industrial furnaces, combustion engines, and oil- or gas-fired heating [7–9]. Various approaches for NO_x removal have been suggested, such as plasma-assisted catalysis, solid–liquid adsorption, and catalytic/non-catalytic reduction [10–12]. However, these processes treat NO_x only at the emission source where the

concentrations of NO_x are in hundreds of ppb and necessitate the use of high temperatures or complex tools for abatement. Photocatalytic oxidation is an effective alternative for NO_x removal at sub-ppb levels under ambient atmospheric conditions. Coating a photocatalyst on concretes and buildings is expected to effectively remove NO_x from the air at a low cost through the utilization of renewable solar energy. In addition, combining photocatalysis with one of the conventional approaches mentioned above is expected to provide a new pathway for the effective removal of large amounts of NO_x from industrial flue gas. However, the limited visible light absorption and low NO_x adsorption capacity of currently available photocatalysts hamper their utilization in practical NO_x oxidation.

The unique characteristics of graphitic carbon nitride (g-C₃N₄) include non-toxicity, high chemical and thermal stability, facile

E-mail address: pamama@ksu.edu (P.B. Amama).

^{*} Corresponding author.

synthesis, remarkable light absorption (band gap of 2.7 eV), and low cost [13–16], rendering it a potential visible light active photocatalyst. However, the photo-reactivity of g-C₃N₄ is hampered by the high recombination rate of photo-induced electron-hole pairs [17,18]. TiO₂ is the most widely used photocatalyst due to its low-cost, facile synthesis, activity under UV light, and stability [19-25]. Utilizing TiO2 as a cophotocatalyst with g-C₃N₄ is an effective route to mitigate charge carrier recombination and boost the overall photocatalytic activity. Charge transfer between g-C₃N₄ and TiO₂ depends on the type of heterojunction between them. In Z-scheme heterojunction, photoexcited electrons in the conduction band (CB) of TiO2 migrate to recombine with the photoexcited holes in the valance band (VB) of g-C₃N₄ at the interface of TiO₂-g-C₃N₄. TiO₂-g-C₃N₄ photocatalyst with a Z-scheme heterojunction has attracted attention because of the good visible light absorption, promoted reaction kinetics, strong reduction and oxidation ability, and improved charge carrier dynamics [26-29]. Z-scheme TiO2-g-C3N4 hybrids have therefore been utilized in a variety of visible light-assisted photocatalytic processes such as CO2 conversion, bacterial inactivation, water treatment, and air purification [30-33].

NO_v photocatalytic oxidation is a multistep reaction involving the conversion of NO (g) to NO₂ (g) followed by the conversion of NO₂ to NO_2^- (s). NO_2^- is the solid-state form of NO_x , which accumulate (store) on the photocatalyst surface during the reaction, reducing the number of available adsorption sites for NO or NO2 oxidation and compromising the overall activity of NO_x oxidation. The photocatalyst should have a high NO_x adsorption capacity for effective NO_x oxidation. Unfortunately, TiO₂ and g-C₃N₄ have low NO_x adsorption capacity [34,35], indicating the limitation of TiO2-g-C3N4 hybrid with conventional morphology as a photocatalyst for NO_x oxidation. In fact, the Z-scheme hybrid photocatalyst formed by coupling TiO2 and g-C3N4 showed limited activity in NO_x oxidation under visible light. To overcome this challenge, Papailias et al.[36] proposed the coupling of TiO2-g-C3N4 with a NO_x storage domain such as CaCO₃. Although this domain improves NO_x storage capacity, its presence reduces the amount of the photo-active components (TiO2 and g-C3N4) in the photocatalyst and may subsequently reduce the number of charge carriers. In addition, the NO_x storage domain can intervene between TiO₂ and g-C₃N₄, reducing the quality of the formed Z-scheme junctions and undermining charge carrier transfer. Recently, Hu et al.[37] suggested the utilization of ultralow work function 2D MXene (titanium carbide MXene) as a hole reservoir and NO_x storage domain with TiO₂-g-C₃N₄. In this ternary structure, the MXene is adapted to facilitate charge carrier separation by accepting the holes from TiO2-g-C3N4, and at the same time, serve as a storage domain for the formed NO₃. However, the MXene is characterized by its low stability and tends to speedily oxidize under ambient condition to form TiO2 and carbonaceous compounds, creating obstacles in front of its utilization in practical NO_x oxidation [38]. Further, the transfer of holes from TiO₂ to MXene reduces their oxidation power and, thereby, their ability to oxidize NO_x species. Therefore, an alternative approach is required to design TiO₂-g-C₃N₄ with high NO_x adsorption capacity while maintaining its intrinsic properties.

 NO_x oxidation is not only controlled by NO_x adsorption capacity but also by H_2O adsorption on the photocatalyst surface- H_2O plays a key role in NO_x oxidation as it traps the photoexcited holes to form active radicals (\bullet OH), which is essential for NO_x oxidation. Therefore, a high concentration of H_2O is expected to boost NO_x oxidation. However, H_2O possesses higher polarity than NO or NO_2 , which can consequently displace them from the photocatalyst surface during the reaction impeding their oxidation. As a result, there is a huge inconsistency in the literature regarding the role of H_2O in NO_x oxidation [39–42]. Although recent studies examined NO_x oxidation by Z-scheme TiO_2 -g- C_3N_4 , the correlation between H_2O concentration and photocatalytic NO_x oxidation remains unclear and yet to be explored.

Recently, hierarchical porous materials have appeared as an appealing family of functional structures in sensing, separation, catalysis/photocatalysis, biomedicine, adsorption, and energy storage

[28,43-45]. Due to their accessible structure, high mass capacity, multiscale porosity, and large surface area, these hierarchical materials are efficient in adsorbing and hosting reaction species. Hence, we hypothesize that coupling hierarchical porous TiO2 with g-C3N4 will lead to the formation of a hybrid photocatalyst with high NO_x adsorption capacity while reducing charge carrier recombination in g-C₃N₄, and hence, exhibit effective NO_x oxidation under visible light. Herein, a hierarchical macro-mesoporous structure composed of Z-scheme TiO₂-g-C₃N₄ hybrid embedded in parallel TiO2 channels was synthesized and used for the first time in NO_x photocatalytic oxidation in a continuous flow reactor. The unique structure of the photocatalyst provides efficient channels for NO_x adsorption and storage of NO_x oxidation product (i.e., $NO_3^-(s)$). The photocatalytic reaction was carried out under concurrent exposure to blue and green lights (cyan light) and 50% relative humidity (RH), which is representative of outdoor humidity levels in most urban cities, as shown in our previous study [41]. DeNO_x index is used to evaluate the overall NO_x oxidation activity by considering both NO conversion and NO2 formation. To develop a mechanistic understanding of photocatalytic NO_x oxidation that will benefit the practical application of the technology, we also investigated the impact of RH on photocatalytic NO_x reaction. The novelty of this work lies in (1) enabling visible lightinduced photoconversion of NO to nitrate rather than NO2 via adapting the photocatalyst structure for effective NO_x adsorption and (2) unraveling the impact of humidity on NO_x oxidation by TiO₂-g-C₃N₄. This study is expected to advance the implementation of photocatalysis as an alternative or a complement to the conventional NO_x abatement techniques.

2. Experimental section

2.1. Photocatalyst synthesis

The TiO2-g-C3N4 heterojunction photocatalyst was synthesized following a procedure reported elsewhere [28]. In brief, the first step involved using a sol-gel process to form the porous TiO₂ framework. About 20 mL of tetrabutyl titanate (Sinopharm Chemical Reagent Co., Ltd., China) was stepwise poured into distilled water (200 mL) and incubated for 36 h at 25 °C. TiO2 precipitate was filtered, rinsed, and dried in an oven at 60 °C for 12 h. This resulted in a dry TiO2 powder with a hierarchical internal structure consisting of aligned macrochannels and mesoporous TiO2 walls. In the second step, 3.0 g of melamine precursor was dispersed in hot distilled water (100 mL) and mixed with 0.50 g of the hierarchical TiO₂ powder. The solution was dried in an oven at 100 °C for 12 h, and the resultant powder was calcined at 550 °C for 2 h under air to yield a yellow-colored TiO₂-g-C₃N₄ photocatalyst. g-C₃N₄ and TiO₂ porous powders were prepared by calcining the melamine precursor and the dried white TiO₂ precipitate after step 1, respectively, at 550 °C for 2 h. The physical properties of the photocatalysts and their optical microscopic images are included in Table S1 and Figure S1, respectively.

2.2. Characterization

The morphology of the samples was characterized using Topcon/ISI/ABT DS 130F field emission scanning electron microscope (FESEM) (Akashi Beam Technology Corporation, Tokyo, Japan) and Tecnai Osiris (Scanning) Transmission Electron Microscope operating at 200 kV (FEI, Hillsboro, OR, USA). The crystal structure of the photocatalysts was examined using Bruker AXS D8 Advance Discover Diffractometer (Bruker Corporation, Karlsruhe, Germany) with a Cu K α radiation of wavelength 0.15418 nm and a detector slit width of 1 mm. XRD reference spectra from Joint Committee on Powder Diffraction Standard (JCPDS) were used for analysis. The composition of the samples was determined using a Thermogravimetric Analyzer (TGA) Q50 system (TA Instruments - Waters LLC, New Castle, DC) at room temperature to 900 °C in an air atmosphere. The optical properties of the photocatalysts

were characterized using Cary 500 UV-VIS-NIR spectrophotometer with a diffuse reflectance accessory (Agilent Technologies, CA, USA). The surface chemical composition was characterized using a PHI 5000 Versa XPS system (Chanhassen, MN) with a monochromatized Al Kα source (1486.7 eV). All the XPS spectra were obtained using a 400 μ m spot size. 200 eV pass energy with 1 eV step was used to collect the survey scans. 50 eV pass energy with 0.1 eV step was utilized to collect the highresolution spectra. A convolution of Gaussian and Lorentzian peaks was used to represent the fitted peak, while the background was subtracted by the Shirley function. The standard sp² C 1 s peak at 284.80 eV was used to charge correct the XPS spectra. Raman spectra were acquired with a DXRTM Raman microscope (Thermo Fisher Scientific, Madison, WI) with a 780 nm laser at a power of 1 mW, using a 10 \times objective lens with a slit width of 25 μm . Multimode microplate reader SpectraMax i3x was used to acquire photoluminescence spectra over the range of 400-700 nm using different excitation wavelengths.

2.3. Photocatalyst performance evaluation

2.3.1. Preparation of film photocatalysts

Samples were ground and dispersed in ethanol (30 mg/ml) by ultrasonication. Each solution was dropped onto a glass slide (37.5 cm 2) and cast to 250 μ m thin film by the doctor blade method. The physical characteristics of the films are summarized in Table S2. The slides coated with the photocatalysts were dried under ambient conditions before subsequent usage.

2.3.2. Reactor configuration

A continuous-flow reactor built following ISO standards made of steel and equipped with a quartz glass window to allow light-photocatalyst interaction was used to perform the NO_x photocatalytic oxidation reaction. Two gas cylinders were connected to the reactor, 100 ppm NO in N_2 and air. The flow rate of gases to the reactor was monitored by mass flow controllers. The humidity on the inlet gas mixture was measured by a sensor-push HT1 humidity sensor. A chemiluminescent 42C Low Source analyzer (Thermo Fisher Scientific) was employed to measure the concentrations of NO and NO_2 during reaction time.

2.3.3. Activity measurement

A photocatalyst coated on a glass slide was placed in a sample holder and loaded into the reactor. 1.0 ppm NO was introduced into the reactor at a total airflow of 1000 sccm and 50% relative humidity and allowed to equilibrate. The reaction was then commenced by light exposure and continued for 30 min. The concentrations of NO and NO $_2$ were calculated by taking the average of all the data obtained during the oxidation reaction.

3. Results and discussion

The morphology of TiO2 and TiO2-g-C3N4 was studied using FESEM. The ${\rm TiO_2}$ possesses a unique architecture of aligned channel-like pores of about 2.5 µm in diameter and up to 20 µm in length with walls that are porous (Fig. 1 a and b). BET analysis revealed that TiO2 comprises mesopores of 2-8 nm. The aligned open channels and combined macromesopores are expected to facilitate faster diffusion of gaseous phase NO_x. As observed in Fig. 1b, a smaller portion of TiO₂ exists as spherical nanoparticles inside the aligned macropores. In the TiO₂-g-C₃N₄ hybrid, the aligned macropores of TiO₂ were partially filled, and the TiO₂ walls were coated uniformly with g-C₂N₄ (Fig. 1 c and d). The aligned pores of TiO₂ facilitated the homogeneous coverage of g-C₃N₄ throughout the pore surfaces by allowing the precursors of g-C₃N₄ to infiltrate into the pores easily. The presence of g-C₃N₄ inside the macropores reduces their diameter to about 1.8 µm. The TEM image in Fig. 1e shows that the spherical TiO2 nanoparticles are intimately coupled with g-C3N4. The intimate interaction between TiO2 and g-C3N4 is further demonstrated by the HRTEM image (Fig. 1f), in which TiO₂ nanoparticles are anchored on g-C₃N₄. This type of interaction between TiO₂ and g-C₃N₄ is essential for forming a highly effective Z-scheme heterojunction. Both the porous structure and effective heterojunction of the TiO2-g-C3N4 hybrid make it suitable as an efficient photocatalyst for NO_x oxidation.

The isotherms of N_2 adsorption—desorption and distributions of pore size of TiO_2 , g- C_3N_4 , and TiO_2 -g- C_3N_4 are shown in Fig. 2a and b. Based on the determination of IUPAC [46], all samples showed Type IV-isotherms, proposing the presence of mesopores. The g- C_3N_4 showed an H3-type hysteresis loop isotherm, signalizing the presence of "slit-like" pores [28]. Conversely, TiO_2 showed an isotherm with an H2-type

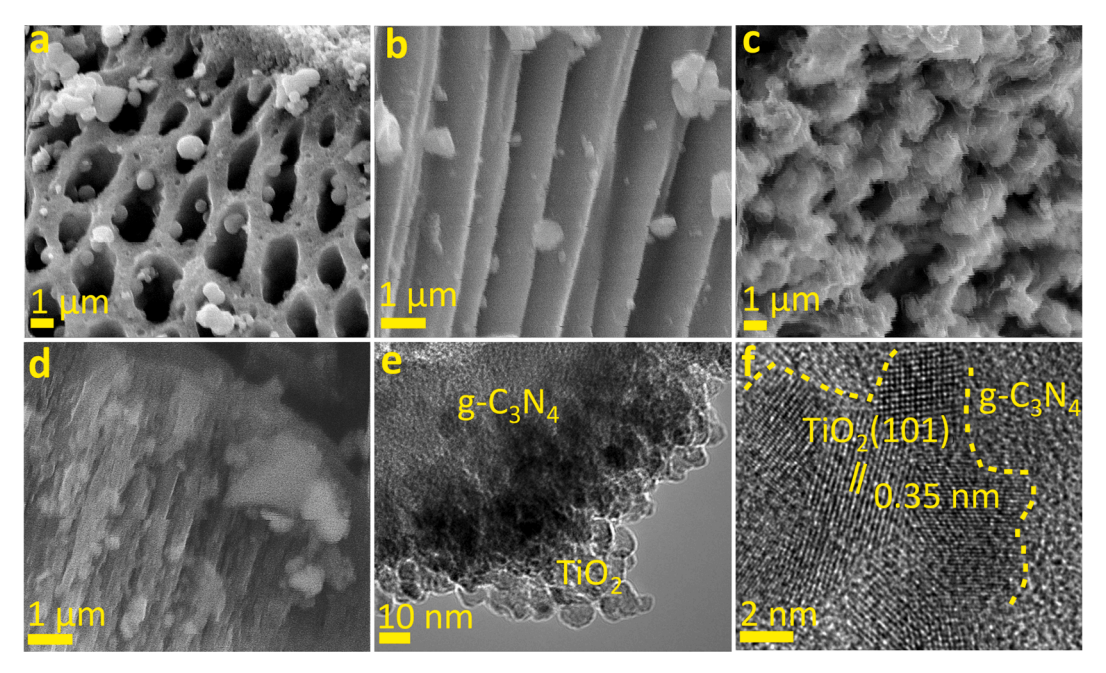


Fig. 1. Morphological characterization of photocatalysts: (a) an SEM image of TiO_2 surface, (b) a cross-sectional SEM image of TiO_2 shown in (a), (c) an SEM image of TiO_2 -g-C₃N₄ surface, (d) a cross-sectional SEM image of TiO_2 -g-C₃N₄ shown in (c), (e) a TEM image of the interface between TiO_2 and g-C₃N₄ in TiO_2 -g-C₃N₄, and (f) the HR-TEM of the interface in (e).

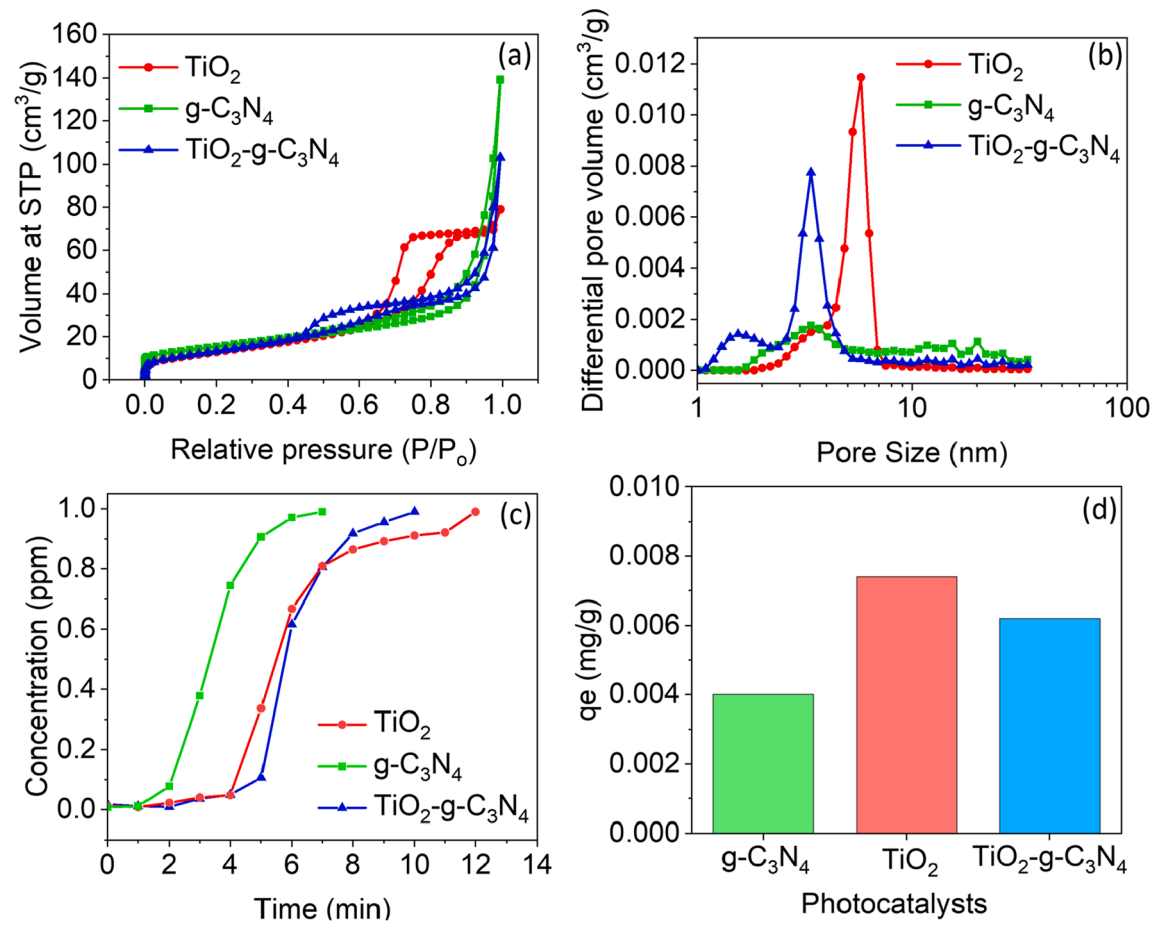


Fig. 2. (a) N_2 adsorption–desorption isotherms of TiO_2 , $g-C_3N_4$, and $TiO_2-g-C_3N_4$. (b) Pore size distributions of TiO_2 , $g-C_3N_4$, and $TiO_2-g-C_3N_4$. (c) Isothermal NO adsorption profiles of TiO_2 , $g-C_3N_4$, and $TiO_2-g-C_3N_4$ and (d) a histogram of their NO adsorption capacity.

hysteresis loop, attributed to the "ink-bottle-like" pores likely formed between the TiO $_2$ sphere in the aligned channels of the hierarchical structure [28]. Interestingly, TiO $_2$ -g-C $_3$ N $_4$ demonstrated a unique structure represented by a hysteresis loop with a combination of H2–and H3-type isotherms. The H2-type loop in the pressure range of 0.4–0.8 is attributed to the "ink-bottle-like" structure from the TiO $_2$ channel occupied with TiO $_2$ /g-C $_3$ N $_4$ aggregates. The H3-type loop in the pressure range of 0.9–1.0 is ascribed to "slit-shaped" pores between the connected structures. TiO $_2$ -g-C $_3$ N $_4$ exhibited a slightly higher surface area (50.4 m 2 /g) than the pristine g-C $_3$ N $_4$ (48.5 m 2 /g). In addition, as depicted in Table S1, TiO $_2$ -g-C $_3$ N $_4$ has a larger mesopore volume (0.0011 cm 3 /g) than g-C $_3$ N $_4$ (0.0008 cm 3 /g). The increase in the pore volume of g-C $_3$ N $_4$ upon coupling with TiO $_2$ is crucial for storing NO $_x$ species and minimizing NO $_2$ formation.

Fig. 2c shows the isothermal adsorption behavior of g-C₃N₄, TiO₂, and TiO₂-g-C₃N₄. NO is used as a representative of NO_x. All samples showed breakthrough time, indicating the favorable NO adsorption on them. The breakthrough time is defined as the time needed to detect NO within the effluent. Generally, the longer the breakthrough time, the better the storage capacity of a catalyst. The breakthrough time of TiO₂ and TiO₂-g-C₃N₄ was longer than that of g-C₃N₄, indicating their high NO adsorption capacity. Interestingly, TiO₂-g-C₃N₄ exhibited almost identical breakthrough time to TiO₂, suggesting coupling g-C₃N₄ and TiO₂ as an efficient pathway to form a photocatalyst with high NO adsorption capacity. It is also observed that the NO saturation times of TiO₂ (12 min) and TiO₂-g-C₃N₄ (10 min) are longer than that of g-C₃N₄ (7 min), further validating the ability of TiO₂ and TiO₂-g-C₃N₄ to adsorb NO effectively. The NO adsorption capacity of the photocatalyst samples was estimated using Equations (1) and (2) [47], and the results are

shown in Fig. 2d.

$$qe = \frac{C_o \times M_{NO} \times P \times F \times S \times 10^{-3}}{R \times T \times W}$$
 (1)

$$S = \int_0^t (1 - \frac{C_{NO}}{C_0}) dt$$
 (2)

where q_e is the NO adsorption capacity (mg/g), C_0 is the inlet NO concentration (ppm), P is the reaction pressure (Pa), M_{NO} is the NO molar mass (30 g/mol), F is the module flow gas rate (m³/s), T is the reaction temperature (25 °C), R is the ideal gas constant (8.314 J/mol·K), S is the integrated area of the adsorption curve, and W_{cat} is the catalyst load mass (g), C_{NO} is the outlet NO concentration (ppm), and t is the adsorption time (s). The results reveal that the adsorption capacity of TiO_2 (0.0070 mg/g) and TiO_2 -g- C_3N_4 (0.0060 mg/g) is higher than that of g- C_3N_4 (0.0038 mg/g). This observation further confirms the improvement in the NO_x adsorption capacity of g- C_3N_4 upon coupling with TiO_2 . Therefore, TiO_2 -g- C_3N_4 is expected to effectively store NO oxidation products during the photocatalytic reaction.

XRD is used to probe the crystal structure of the samples, as depicted in Fig. 3 a. The TiO₂ sample showed the characteristic diffraction peaks at 25.3°, 36.9°, 37.8°, 38.6°, 48.0°, 53.9°, 55.1°, 62.1°, 62.7°, and 68.7° that correspond to (101), (103), (004), (112), (200), (105), (211), (213), (204), and (116) planes of anatase TiO₂ (JCPDS# 21–1272). The g-C₃N₄ sample showed two characteristic diffraction peaks at 13.1° and 27.6° corresponding to the (100) and (002) planes of g-C₃N₄, respectively. The TiO₂-g-C₃N₄ hybrid sample has diffraction peaks at 25.3°, 13.1°, and 27.6° that are characteristic of both g-C₃N₄ and TiO₂, confirming the formation of the hybrid structure. The presence of weak

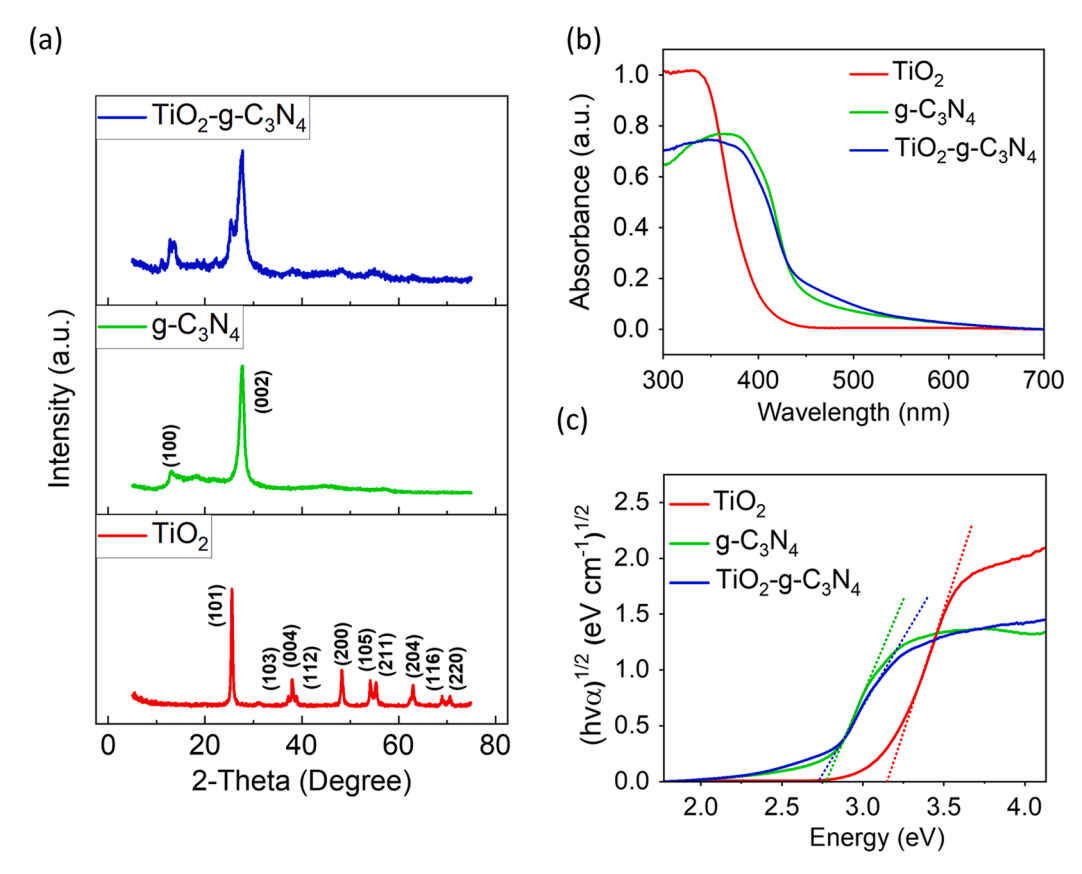


Fig. 3. (a) X-ray diffraction patterns of TiO_2 , g- C_3N_4 , and TiO_2 -g- C_3N_4 ; (b) UV–Vis diffuse reflectance spectra of TiO_2 , g- C_3N_4 , and TiO_2 -g- C_3N_4 ; (c) Tauc plots from UV–Vis spectra shown in (b) of TiO_2 (band gap: 3.15 eV), g- C_3N_4 (band gap: 2.77 eV), and TiO_2 -g- C_3N_4 ((band gap: 2.71 eV).

 TiO_2 peaks and strong g-C₃N₄ peaks suggest that a higher composition of g-C₃N₄ is present in the TiO_2 -g-C₃N₄. This is well supported by the TGA curves shown in Figure S2, where the composition of TiO_2 -g-C₃N₄ was determined to be 79.5% of g-C₃N₄ and 20.5% of TiO_2 . The derivation of elemental composition from TGA curves can be found in Table S3.

UV–Vis diffuse reflectance spectroscopy is employed to study the optical properties of the samples, and the results are presented in Fig. 3b. Compared with TiO_2 , whose absorption is restricted to the UV region, the absorptions of $g-C_3N_4$ and $TiO_2-g-C_3N_4$ are red-shifted with a noticeable shoulder in the region between 460 and 560 nm. The optical band gaps of the samples, shown in Fig. 3c, were estimated using Tauc and Davis — Mott method according to Equation (3):

$$(\alpha h \nu)^{\frac{1}{2}} = A \left(h \nu - E_g \right) \tag{3}$$

where α is the coefficient of absorption, E_g is the band gap, ν is the frequency of radiation, h is Planck's constant, and A is the proportionality constant. TiO₂ has an absorption edge at 393.6 nm with a band gap

of 3.15 eV. The band gap of g-C₃N₄ was 2.77 eV, corresponding to an absorption edge at 447.6 nm. The absorption edge of the hybrid $\rm TiO_2$ -g-C₃N₄ extends into the visible region with a band gap of 2.71 eV, corresponding to an absorption edge of 457.6 nm, which is lower than that of $\rm TiO_2$ by 0.44 eV. The narrower band gap and stronger absorption at longer wavelengths of the hybrid sample are essential for photoexcitation by visible light irradiation.

PL spectroscopy was used to investigate the samples' fluorescence, and the results are shown in Fig. 4. The samples were excited by different wavelengths (460, 480, 500, 520, 540, and 560 nm). We chose these wavelengths to verify the UV–Vis data (Fig. 3b and c) that indicate the ability of g-C₃N₄ and TiO₂-g-C₃N₄ to absorb light in the region between 460 and 560 nm. As shown in Fig. 4b, the g-C₃N₄ showed high fluorescence in this region, unlike TiO₂ with limited absorption (Fig. 4a). This observation confirms the generation of charge carriers on g-C₃N₄ under visible light exposure. TiO₂-g-C₃N₄ exhibited a slightly lower fluorescence intensity than g-C₃N₄ (Fig. 4c). Because the fluorescence is generated from electron-hole recombination, the reduction

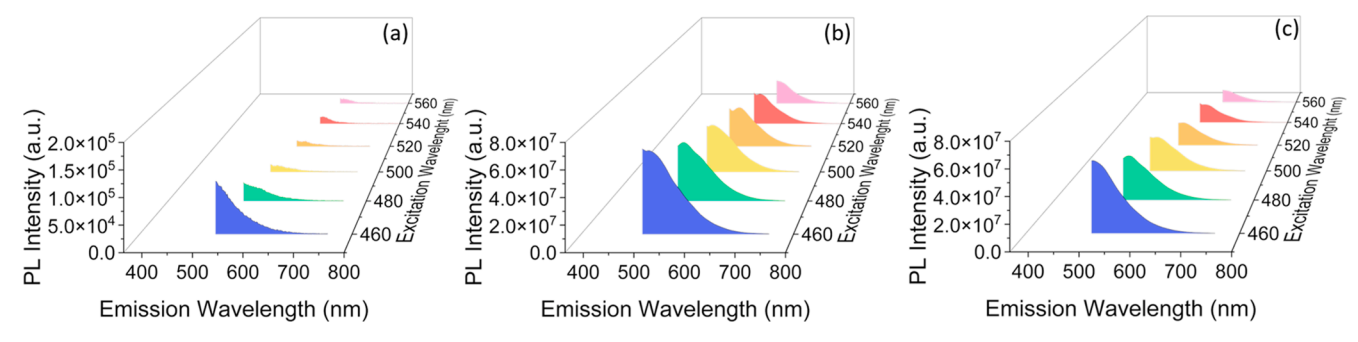


Fig. 4. Photoluminescence spectra of TiO2 (a), g-C3N4 (b), and TiO2-g-C3N4 (c) hybrids using lights of various wavelengths.

in its intensity indicates the separation of the charge carriers through the Z-scheme junction formed between TiO_2 and g- C_3N_4 .

XPS analysis was carried out to investigate the surface chemistry of the samples. Figure S3 shows the survey spectra of the photocatalysts. Table S4 summarizes the atomic concentration (at%) calculated from the survey spectra. The high-resolution spectra of C 1 s, N 1 s, and Ti 2p are shown in Figure S4. The carbon signal in TiO₂ is attributed to the adventitious carbon (Fig. S4a). The peak at 284.8 eV in the deconvoluted C 1 s spectrum of g-C₃N₄ correspond to the C-C bond from graphitic carbon residues, whereas the peaks at 286.5 eV and 288.3 eV are attributed to C-NH2 and C = N-C from g-C3N4 backbone, respectively [28,48]. Similarly, the TiO₂-g-C₃N₄ was fitted into three peaks at 284.8 eV, 286.4 eV, and 288.2 eV, confirming the presence of g-C₃N₄ in the hybrid catalyst. Fig. S4b shows the high-resolution N 1 s spectrum of the samples. The TiO $_2$ has \sim 0.9 at% of N in the sample, which may be attributed to the surface-adsorbed nitrogen species from the atmosphere. The N 1 s spectra of the g-C₃N₄ and TiO₂-g-C₃N₄ samples were deconvoluted into two peaks at 398.7 eV and 400.2 eV, corresponding to the sp² hybridized pyridinic nitrogen (C = N-C) and tertiary nitrogen (N-C) C_3) confirming the structure of g- C_3N_4 [48]. There was a third peak located at 404.5 eV, which could be due to the features of amino functional groups with hydrogen on the g-C₃N₄ [49]. Fig. S4c shows the Ti 2p high-resolution peaks of TiO2, g-C3N4, and the hybrid TiO2-g-C3N4 samples. The Ti 2p spectra of both TiO2 and TiO2-g-C3N4 samples were deconvoluted into a pair of peaks at binding energies of 458.7 and 464.4 eV, ascribed to the Ti $2p_{3/2}$ and Ti $2p_{1/2}$ doublet of Ti⁴⁺ states ascribed to TiO₂ [50].

High-resolution XPS O1s spectra of TiO2, g-C3N4, and TiO2-g-C3N4 before and after photocatalytic reactions are shown in Fig. 5. TiO₂ spectrum before the reaction (Fig. 5a; top) was deconvoluted into two peaks at the binding energy (BE) of 529.2 and 531.1 eV corresponding to Ti-O and Ti-OH, respectively [51]. g-C₃N₄ spectrum before the reaction (Fig. 5b; top) showed the presence of a dominant peak at 532.2 eV attributed to surface-adsorbed H2O. The detection of molecularly adsorbed H₂O on g-C₃N₄ by XPS is supported by the findings of previous studies [52-55]. However, few other studies attributed this peak to chemisorbed oxygen on the g-C₃N₄ surface [56,57]. TiO₂-g-C₃N₄ spectrum before the reaction (Fig. 5c; top) was deconvoluted into two peaks at 529.9 eV and 532 eV attributed to Ti-O and Ti-OH, respectively [58]. The presence of -OH groups on the catalyst surface is essential for trapping the photoexcited charge carriers (particularly the holes) and subsequently forming active radicals for NO_x oxidation (discussed in detail later).

Further characterization of the composite was done by Raman spectroscopy using a 780 nm laser (Figure S5). Notably, g-C₃N₄ has a strong fluorescence background mixed in the Raman spectra even using a 780 nm laser; however, characteristic peaks corresponding to g-C₃N₄ and TiO₂ can still be observed on top of the high background. TiO₂ has bands at 141 cm⁻¹ (E_g), 194 cm⁻¹ (E_g), 394 cm⁻¹ (B_{1g}), 513 cm⁻¹ (A_{1g}, B_{1g}), and 637 cm⁻¹ (E_g) characteristic of the anatase phase [59,60]. The phase composition is consistent with XRD data showing only the anatase phase. The g-C₃N₄ showed bands at 748 cm⁻¹, 1115 cm⁻¹, 1152 cm⁻¹, 1232 cm⁻¹, and 1308 cm⁻¹ corresponding to stretching vibration modes of C-N characteristic of melamine [61]. The bands at 707 cm⁻¹ and $1558\,\mathrm{cm}^{-1}$ can be attributed to the breathing modes of the s-triazine ring and the stretching modes of the C = N bond, respectively [62,63]. It is to be noted that the strong fluorescence background was from the g-C₃N₄, consistent with a previous study [64]. In the Raman spectra of TiO₂-g-C₃N₄ composite material, Raman bands corresponding to both TiO₂ and g-C₃N₄ could be observed, indicating the presence of both TiO₂ and g-C₃N₄. The E_g vibrational mode of anatase phase TiO₂ was shifted to higher wavenumbers by 6 cm⁻¹ in the composite, which could be due to strain induced by the coating of g-C₃N₄, indicating a stronger interaction between g-C₃N₄ and TiO₂ and/or by the C, N doping in TiO₂ [65].

4. NO_x photocatalytic oxidation

Fig. 6a shows the NO conversion of TiO_2 , $g-C_3N_4$, and TiO_2 - $g-C_3N_4$ under simultaneous exposure to blue and green light and at 50% RH. NO conversion of TiO_2 - $g-C_3N_4$ is 34 %, four times higher than TiO_2 (7 %) and two times higher than $g-C_3N_4$ (17 %). This indicates that coupling TiO_2 with $g-C_3N_4$ fosters NO conversion of $g-C_3N_4$. Photocatalytic NO_x oxidation typically involves the formation of NO_2 , a more toxic compound than NO; therefore, an effective photocatalyst should minimize the release of NO_2 into the atmosphere while maintaining reasonable conversion of NO_2 and then store a significant portion of the formed NO_2 on the surface of the catalyst as nontoxic NO_3^- . Hence, the activity of a photocatalyst in NO_x oxidation should be evaluated by considering both NO conversion and NO_x storage selectivity.

 $DeNO_x$ index, a parameter that measures the overall activity of a photocatalyst in NO_x removal by considering both NO conversion and NO_x storage selectivity, is used to quantify the performance of TiO_2 , $g-C_3N_4$, and $TiO_2-g-C_3N_4$. This index was first suggested by Bloch et al. [7], and is based on the assumption that the total toxicity of air is affected three times more by NO_2 than NO. A photocatalyst demonstrates a NO_x

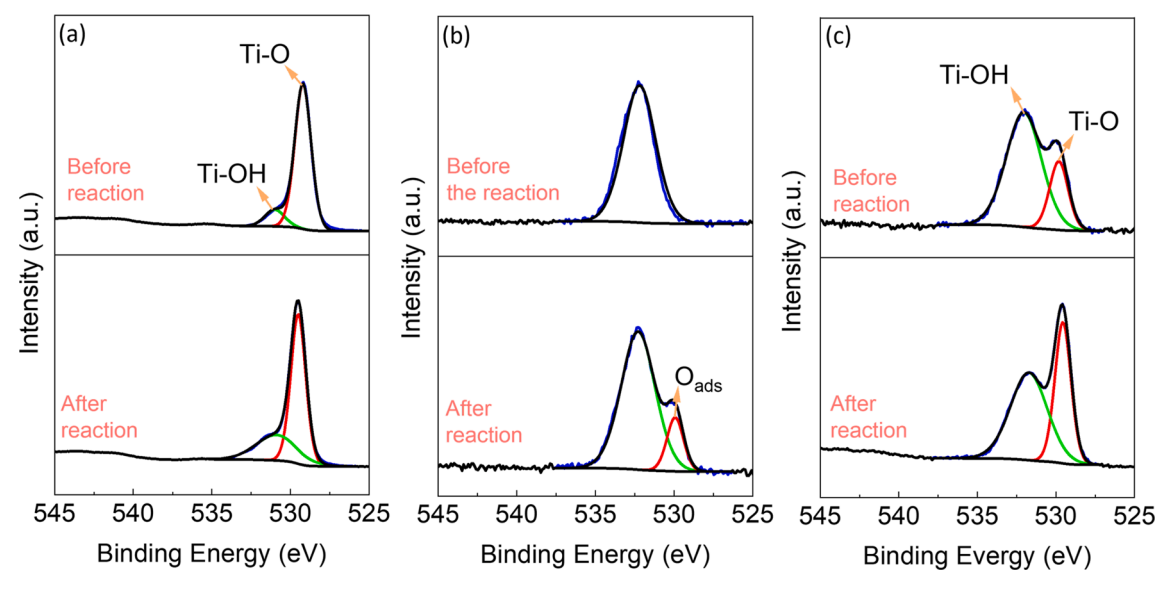


Fig. 5. High-resolution O1s XPS spectra of TiO₂ (a), g-C₃N₄ (b), and TiO₂-g-C₃N₄ (c) before (top) and after (bottom) the photocatalytic reaction.

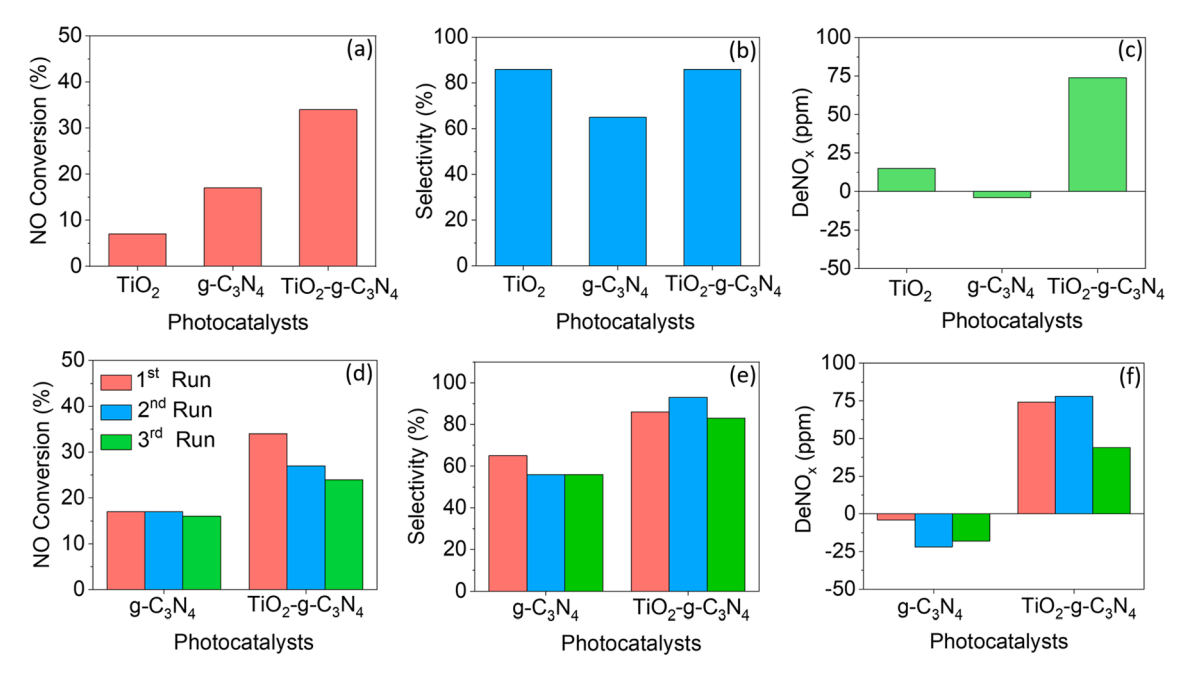


Fig. 6. Photocatalytic oxidation of NO_x using TiO_2 , $g-C_3N_4$, and $TiO_2-g-C_3N_4$ under cyan light and 50% RH: (a) NO conversion, (b) NO_x storage selectivity, and (c) $DeNO_x$ index. NO_x oxidation using the recycled $g-C_3N_4$ and $TiO_2-g-C_3N_4$ photocatalysts (three consecutive cycles): (d) NO conversion, (e) NO_x storage selectivity, and (f) $DeNO_x$ index.

"purification effect" when it possesses a positive $DeNO_x$ index and hence is preferred. On the other hand, a photocatalyst shows a NO_x "toxification effect" when it has a negative $DeNO_x$ index and therefore is undesired.

The DeNO_x index and NO_x storage selectivity of the photocatalysts were calculated by using Equations (4), (5), and (6) [7].

$$\xi = \frac{(c_d - c_i)\dot{V}p}{\omega ART} \tag{4}$$

Selectivity =
$$\frac{\xi_{NOx}}{\xi_{NO}}$$
 (5)

$$DeNO_x index = \xi_{NO_x} \left(3 - \frac{2}{S} \right) \tag{6}$$

where ξ is the photonic efficiency of NO_x species; c_d is the species concentrations in the dark (ppm); c_i is the species concentrations under illumination (ppm); \dot{V} is the volumetric flow rate; p is the pressure in the system (1 atm); φ is the photon flux at the photocatalyst surface (photon/m² s; dependent on light wavelength and intensity); A is the catalyst irradiated area; R is the gas constant; and T is the temperature.

 TiO_2 -g- C_3N_4 has a purification effect as it exhibits high NO_x storage selectivity, reasonable NO conversion (34 %,), and a positive $DeNO_x$ index (Fig. 6 b and c); it is therefore suitable for NO_x oxidation. In contrast, g- C_3N_4 exhibited a lower selectivity towards NO_x storage and a negative $DeNO_x$ index (Fig. 6b and c) with low NO conversion (17 %) as shown in Fig. 6a, indicating its toxification effect and its unfeasibility for NO_x oxidation. It is noted that although TiO_2 showed a slightly positive $DeNO_x$ index and high NO_x storage selectivity (Fig. 6b and c), it suffered from very low NO conversion (7 %), confirming its ineffectiveness as a NO_x oxidation photocatalyst.

To evaluate the reusability and long-term activity of the photocatalysts, we conducted three consecutive photocatalytic NO_x oxidation experiments using $g\text{-}C_3N_4$ and $TiO_2\text{-}g\text{-}C_3N_4$, and the results are shown in Fig. 6. The $DeNO_x$ index and selectivity of recycled TiO_2 are not shown because the NO conversion of recycled TiO_2 is approximately zero. The selectivity and $DeNO_x$ index of $TiO_2\text{-}g\text{-}C_3N_4$ slightly decreased after each cycle (Fig. 6d), likely because of the accumulation of NO_x

photooxidation product on the catalyst surface and consequent consumption of NO_x adsorption sites. Nevertheless, the recycled TiO_2 -g- C_3N_4 exhibited high selectivity and positive $DeNO_x$ index (Fig. 6e and f), maintaining its purification effect. g- C_3N_4 experienced a decrease in selectivity after recycling with an increase in the negativity of its $DeNO_x$ index (Fig. 6 e and f), indicating the increase in its toxification effect and further affirming its unsuitability for NO_x oxidation. Comparing the performance of TiO_2 -g- C_3N_4 with other TiO_2 -based photocatalysts in the literature is challenging because of the variation in reactor design and reaction conditions. Nevertheless, to give the reader an idea about the performance of TiO_2 -based photocatalysts in NO_x oxidation, we summarized NO conversion, selectivity, and $DeNO_x$ index along with reaction conditions in Table~1. TiO_2 -g- C_3N_4 showed a high $DeNO_x$ index and selectivity at low photocatalyst concentration, while demonstrating comparable conversion of NO.

The difference in the photocatalytic activity of TiO_2 , g- C_3N_4 , and TiO_2 -g- C_3N_4 is explained by examining the mechanism of NO_x oxidation, which is split into three steps [42,66,67]: (1) the interaction of light and photocatalyst and the consequent formation of charge carriers (Equation (7)); (2) the reaction between the formed charge carriers and oxygencontaining molecules (O_2 and O_2 - O_3 -

$$TiO_2 + hv \rightarrow TiO_2(h^+ + e^-) \tag{7}$$

$$TiO_2(h^+) + H_2O \rightarrow TiO_2 + {}^{\bullet}OH + H^+$$
(8)

$$Ti - OH + h^{+} \rightarrow Ti^{+} + {}^{\bullet}OH \tag{9}$$

$$TiO_2(e^-) + O_2 \rightarrow TiO_2 + {}^{\bullet}O_2^-$$
 (10)

$$NO + {}^{\bullet}O_2^- \rightarrow NO_3^- \tag{11}$$

$$NO+^{\bullet}OH \rightarrow HNO_2$$
 (12)

$$HNO_2 + {^{\bullet}OH} \rightarrow NO_2 + H_2O \tag{13}$$

Table 1Performance of state-of-the-art photocatalysts at room temperature under relative humidity of 40 to 50%.

Catalyst	Light wavelength (nm)	Catalyst amount (mg)	Inlet NO (ppm)	NO conversion (%)	Selectivity (%)	DeNO _x (ppm) ¹	DeNO _x ²	Ref.
P25	_	300	8	_	27.8	-3689	_	[7]
FeTi4	315-1050	0.55	0.1	23	63	_	_	[71]
25Ca/Ti	315-400	900	1	46	77	_	0.14	[42]
70Al/Ti	315-400	900	1	42	64	_	-0.03	[42]
mpg-CN500	400-700	200	1	40	83	-	0.20	[72]
$Ti_{0.909}W_{0.091}O_2N_x$	_	300	8	_	90	150	_	[73]
Conventional TiO ₂ -g- C ₃ N ₄	> 400	_	1	20	-	-	0.025	[36]
TiO ₂ -g-C ₃ N ₄	425–515	19	1	35	86	74	0.25	This study

 $^{^{1}\,}$ DeNO $_{x}$ index calculated based on the procedure reported herein.

$$NO+^{\bullet}O_2^- + H^+ \rightarrow NO_2 + ^{\bullet}OH \tag{14}$$

$$NO+^{\bullet}O_{2}^{-} + H^{+} \rightarrow HNO_{3}$$
 (15)

$$NO_2 + {}^{\bullet}OH \rightarrow HNO_3 \rightarrow H^+ + NO_3^-$$
 (16)

The concentration of ROS formed on the surface of TiO_2 is low due to its large band gap and the subsequent poor formation of charge carriers under visible light as depicted in Fig. 7a. We did not observe any significant variation in O1s XPS spectra of TiO_2 obtained before and after the reaction as depicted in Fig. 5a. This observation implies the weak interaction between TiO_2 and surface oxygen-containing species (–OH groups or adsorbed oxygen), likely due to the absence of charge carriers. Therefore, TiO_2 showed low NO oxidation activity. Although g-C₃N₄ has a low band gap and is capable of producing charge carriers under visible light, a significant portion of the carriers undergoes recombination. Therefore, only a few amounts of charge carriers remain alive on g-C₃N₄ to participate in the redox reaction, undermining NO_x oxidation. In addition, the VB edge potential of g-C₃N₄ (+1.63 eV versus NHE) is less

positive than the potential required to oxidize H₂O to •OH (+2.68 versus NHE) or -OH to •OH (+1.99 eV versus NHE). Consequently, the direct formation of •OH on g-C₃N₄ is improbable. In fact, the presence of a dominant peak attributed to the adsorbed H₂O in the O1s XPS spectrum of g-C₃N₄ collected after the reaction (Fig. 5b) indicates the weak interaction between the holes and H2O. In other words, the H2O adsorbed on g-C₃N₄ did not consume by the holes during the reaction. On the other hand, O1s XPS spectrum of g-C₃N₄ obtained after the reaction (Fig. 5b) detects the presence of a peak at 530 eV associated with the adsorbed oxygen [68], likely formed as a result of electron transfer to O_2 . Hence, the NO_x oxidation will be mainly dominated by ${}^{\bullet}O_2^-$, or the so-called electron-meditated mechanism (Equations (10), (11), (14), and (15)). Although a recent study suggests that the ${}^{\bullet}O_2^-$ is crucial to NO_x oxidation through direct conversion of NO to NO₃/HNO₃ [41], this mechanism does not seem proper for g-C₃N₄, evident by its negative DeNOx index. It is important to mention that the formation of $\bullet OH$ cannot be entirely eliminated as there is another pathway for the indirect formation of •OH. This pathway includes the disproportionation of

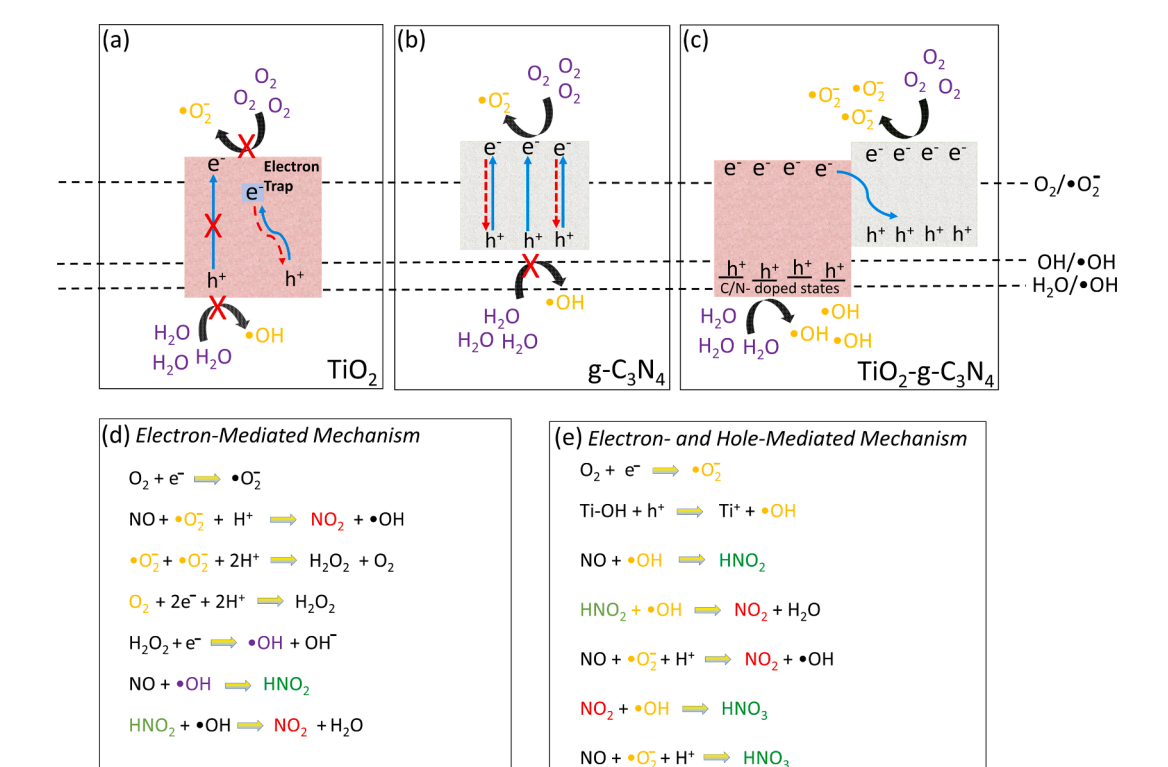


Fig. 7. Schematic diagrams of photo-induced charge carrier formation and subsequent active radicals formed in (a) TiO₂, (b) g-C₃N₄, and (c) TiO₂-g-C₃N₄ under cyan lights. Schematic diagrams of (d) an electron-hole-mediated mechanism and (e) a hole-mediated mechanism of NO_x photocatalytic oxidation.

 $^{^{2}}$ Modified DeNO_x index calculated based on the procedure reported by M. Çağlayan et al. [42].

 ${}^{\bullet}O_2^{-}$ as shown in Equations (17)–(20), in agreement with previous studies [69,70]. The photocatalytic mechanism and electron-mediated mechanism of NO_x oxidation by g-C₃N₄ are shown in Fig. 7b and d, respectively. However, the low concentration of ${}^{\bullet}O_2^{-}$ formed on g-C₃N₄ due to electron-hole recombination undermines its ability to generate a decent amount of ${}^{\bullet}OH$ required for effective NO_x abatement. Furthermore, previous studies suggested that NO_x species are only weakly adsorbed on g-C₃N₄ [35,36], hindering the first step in the photocatalytic reaction (adsorption). Therefore, we conclude that the poor NO_x oxidation activity of g-C₃N₄ is due to its low photonic efficiency and poor adsorption capacity.

$${}^{\bullet}O_{2}^{-} + {}^{\bullet}O_{2}^{-} + 2H^{+} \rightarrow H_{2}O_{2} + O_{2}$$
 (17)

$$O_2 + 2e^- + 2H^+ \rightarrow H_2O_2$$
 (18)

$$H_2O_2 + e^- \rightarrow {}^{\bullet}OH + OH^-$$
 (19)

$$H_2O_2 + hv \rightarrow {}^{\bullet}OH + {}^{\bullet}OH$$
 (20)

In the case of TiO₂-g-C₃N₄, the Z-scheme synergy between g-C₃N₄ and TiO2 allows the migration of photogenerated electrons from TiO2 CB to recombine with the photogenerated holes in g-C₃N₄ VB. This gives rise to the accumulation of electrons in CB of g-C₃N₄ and holes in VB (or inter-band states) of carbon- or nitrogen-doped TiO2; thereby, electronhole separation as depicted in Fig. 7c. It is noted that TiO2 in TiO2-g-C₃N₄ is visible light active due to the presence of inter-band states formed due to carbon and nitrogen doping, as demonstrated previously [28]. CB edge of g-C₃N₄ (-1.17 eV versus NHE) is located above the standard redox potential of $O_2/^{\bullet}O_2^{-}$ (-0.046 eV versus NHE) and CB edge of TiO2 (-0.31 eV versus NHE) [28]. Therefore, the electrons accumulated in CB of g-C₃N₄ possess higher reducing capability than those in CB of TiO₂ to reduce the adsorbed O₂, favoring the formation of \cdot O₂. The energy levels of carbon or nitrogen impurities in TiO2 is located at approximately 2.50 eV, which is more positive than g-C₃N₄ VB (+1.63 eV versus NHE) and the potential required to oxidize OH to \bullet OH (+1.99) [28]. Therefore, the energetic holes in TiO₂ can oxidize NO_x through a hole-mediated mechanism (Equations (9), (12), (13) and (16)), in contrast to g-C₃N₄ in which NO_x oxidation is dominated by electronmediated mechanism (particularly, Equations (10) and (14)). O1s XPS spectrum of TiO₂-g-C₃N₄ (Fig. 5c) confirmed the consumption of -OH groups by the energetic holes during the reaction, evident by the reduction in the intensity of peak associated with this species at BE = 532 eV; whereas the increase in the intensity of peak at BE = \sim 530 eV can be attributed to O2 adsorption similar to that of pure g-C3N4 in Fig. 5b. Therefore, TiO₂-g-C₃N₄ is expected to perform NO_x oxidation by

both the electron- and hole-mediated mechanisms, leading to the formation of a high concentration of ROS (Fig. 7c and e). In addition, the unique structure of TiO_2 -g- C_3N_4 represented by the presence of macro/mesopores provides a suitable structure (as confirmed by N_2 adsorption–desorption isotherms) for the storage of NO_x oxidation products on the catalyst surface, in contrast to g- C_3N_4 . Hence, effective NO_x oxidation is achieved.

To investigate the impact of water adsorption on NO_x photocatalytic oxidation, we conducted further experiments at low humidity (10% RH). Fig. 8a, b, and c show concentration profiles of NO_x during the photocatalytic reaction by TiO2, g-C3N4, and TiO2-g-C3N4 under low and high humidity levels. For proper comparison, the experiments were conducted under blue light to eliminate the impact of catalyst photonic efficiency (ability to form charge carriers), as all catalysts are active under blue light. Under low humidity, we did not observe any significant formation of NO2 by all photocatalysts; NO2 concentration is almost 0 ppm. TiO2 and TiO2-g-C3N4 showed approximately identical NO conversion under low humidity, which is remarkably higher than that of g-C₃N₄. However, under high humidity, the NO conversion activity of TiO₂ significantly declined. It may be ascribed to the formation of bridging hydroxyl groups as a result of the dissociation of water molecules on oxygen vacancies of TiO₂ [34,42]. These groups can capture the photogenerated electrons, boosting their recombination with holes; hence the number of ROS on TiO2 is expected to be low, and this could be the reason for the poor NO conversion observed. g-C₃N₄ showed higher NO conversion under high humidity than under low humidity, with a slight formation of NO2. The formation of NO2 can be attributed to the reduction in the adsorption sites available for NO₂ storage due to H₂O adsorption on g-C₃N₄. Interestingly, TiO₂-g-C₃N₄ showed reasonable NO conversion under high humidity, which is slightly lower than that achieved under low humidity, with a noticeable formation of NO2. Although water dissociation on TiO2 is still possible with TiO2-g-C3N4 under high humidity, the photo-generated electrons are not trapped by the generated bridging hydroxyl groups but transferred to g-C3N4 as explained earlier, leaving holes on TiO2 for photocatalytic NOx oxidation. This indicates that the Z-scheme is vital in enabling both electrons and holes to participate in the photocatalytic reaction, and hinders charge carrier consumption by water-induced charge carrier recombination centers. The increase in the formation of NO2 by TiO2-g-C3N4 under high humidity is ascribed to the adsorption of H2O on the catalyst surface and the consequent reduction in the number of sites available for NO_x storage. In other words, the H₂O occupies the sites available for the adsorption of the generated NO₂, hindering its oxidation and leading to its release into the atmosphere. Nevertheless, the formation of NO2 by

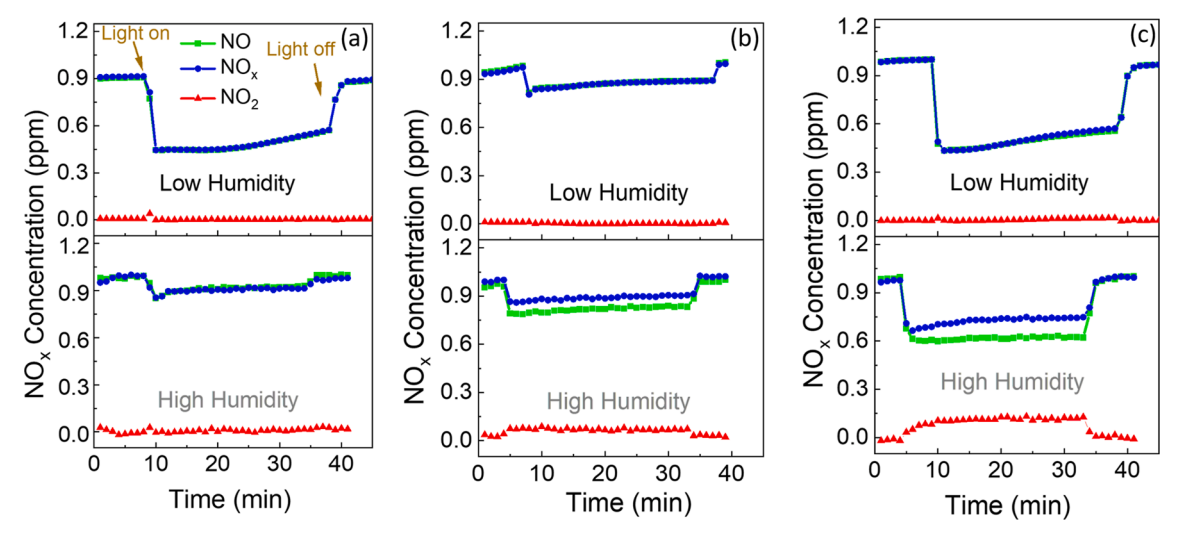


Fig. 8. Representative NO_x oxidation profiles of TiO₂ (a), g-C₃N₄ (b), and TiO₂·g-C₃N₄ (c) under low and high humidity levels and exposure to blue light.

 TiO_2 -g- C_3N_4 under a humid environment should not prevent its utilization in NO_x oxidation since it has a net purification effect, evidenced by its positive $DeNO_x$ index under blue light (Figure S6) and cyan light (Fig. 6c).

5. Conclusions

A hierarchical macro-mesoporous structure composed of Z-scheme TiO₂-g-C₃N₄ hybrid embedded in parallel TiO₂ channels was synthesized and used in photocatalytic NO_x oxidation. The Z-scheme heterojunction formed between TiO2 and g-C3N4 enabled the separation of a large portion of photogenerated charge carriers while maintaining the high reducing power of electrons in g-C₃N₄ CB and high oxidizing power of holes in TiO_2 VB, making it possible for TiO_2 -g- C_3N_4 to perform NO_x oxidation under cyan light. TiO₂-g-C₃N₄ showed NO conversion (37 %) that is four times higher than that of TiO₂ (7 %) and two times higher than that of g-C₃N₄ (17%). TiO_2 -g-C₃N₄ also showed superior NO_x storage capacity and, in turn, has a purification effect, evident by its positive DeNO_v index (+74 ppm) in contrast to g-C₃N₄ with a negative DeNO_v (-4 ppm) and TiO₂ with a slightly positive DeNO_v index (+15 ppm). This study also revealed the impact of humidity on the NO_v oxidation activity of catalysts and proposed possible pathways for the consumption of charge carriers and reduction of NO_x storage sites. Furthermore, detailed photocatalytic mechanisms for NO_x oxidation by g-C₃N₄ and TiO₂-g-C₃N₄ were suggested. The finding of this study is expected to stimulate researchers to utilize hierarchical TiO2-based hybrid photocatalysts in NO_x oxidation and explore their application in practical NO_x abatement under ambient conditions.

CRediT authorship contribution statement

Ahmed Al Mayyahi: Conceptualization, Methodology, Investigation, Writing – original draft, Data curation. Archana Sekar: Investigation, Writing – original draft. Sabari Rajendran: Investigation, Writing – original draft. Shusil Sigdel: Investigation. Lianying Lu: Investigation. Juan Wang: Investigation. Guohong Wang: Investigation. Jun Li: Conceptualization, Data curation, Funding acquisition, Supervision, Validation, Writing – review & editing. Placidus B. Amama: Conceptualization, Validation, Funding acquisition, Data curation, Supervision, Writing – review & editing.

Declaration of Competing Interest

The authors declare that they have no known competing financial interests or personal relationships that could have appeared to influence the work reported in this paper.

Data availability

Data will be made available on request.

Acknowledgements

The study on photocatalysis is partially supported by the National Science Foundation under the NSF CAREER program (Grant No. 1653527). The work by Jun Li's group is partially supported by the National Science Foundation under grant CBET-2054754. The authors thank Prof. Christer Aakeroy at Kansas State University for assisting with TGA measurements, and acknowledge use of the Nebraska Nanoscale Facility supported by the National Science Foundation under Award ECCS: 2025298 and the Nebraska Research Initiative for XPS characterization. The authors thank Dr. Brian Everhart and Prof. Christopher Jones at Kansas State University for assisting with the reactor set up and photocatalyst characterization, respectively.

Appendix A. Supplementary data

Supplementary data to this article can be found online at https://doi.org/10.1016/j.jphotochem.2023.114965.

References

- [1] S.K. Thakrar, S. Balasubramanian, P.J. Adams, I.M.L. Azevedo, N.Z. Muller, S. N. Pandis, S. Polasky, C.A. Pope, A.L. Robinson, J.S. Apte, C.W. Tessum, J. D. Marshall, J.D. Hill, Reducing Mortality from Air Pollution in the United States by Targeting Specific Emission Sources, Environ. Sci. Technol. Lett. 7 (9) (2020) 639–645.
- [2] M. Heidari, M. Tahmasebpoor, S.B. Mousavi, C. Pevida, CO₂ capture activity of a novel CaO adsorbent stabilized with (ZrO₂+Al₂O₃+CeO₂)-based additive under mild and realistic calcium looping conditions, J. CO₂ Util. 53 (2021), 101747.
- [3] M. Heidari, S. Borhan Mousavi, F. Rahmani, P.T. Clough, S. Ozmen, The novel Carbon Nanotube-assisted development of highly porous CaZrO₃-CaO xerogel with boosted sorption activity towards high-temperature cyclic CO₂ capture, Energ. Conver. Manage. 274 (2022), 116461.
- [4] S.B. Mousavi, M. Heidari, F. Rahmani, R. Akbari Sene, P.T. Clough, S. Ozmen, Highly robust ZrO₂-stabilized CaO nanoadsorbent prepared via a facile one-pot MWCNT-template method for CO₂ capture under realistic calcium looping conditions, J. Clean. Prod. 384 (2023), 135579.
- [5] X.i. Gong, A. Kaulfus, U. Nair, D.A. Jaffe, Quantifying O₃ Impacts in Urban Areas Due to Wildfires Using a Generalized Additive Model, Environ. Sci. Tech. 51 (22) (2017) 13216–13223.
- [6] R.-J. Huang, Y. Zhang, C. Bozzetti, K.-F. Ho, J.-J. Cao, Y. Han, K.R. Daellenbach, J. G. Slowik, S.M. Platt, F. Canonaco, P. Zotter, R. Wolf, S.M. Pieber, E.A. Bruns, M. Crippa, G. Ciarelli, A. Piazzalunga, M. Schwikowski, G. Abbaszade, J. Schnelle-Kreis, R. Zimmermann, Z. An, S. Szidat, U. Baltensperger, I.E. Haddad, A.S. H. Prévôt, High secondary aerosol contribution to particulate pollution during haze events in China, Nature 514 (2014) 218–222.
- [7] J.Z. Bloh, A. Folli, D.E. Macphee, Photocatalytic NO_x abatement: why the selectivity matters, RSC Adv. 4 (2014) 45726–45734.
- [8] K. Skalska, J.S. Miller, S. Ledakowicz, Trends in NO_x abatement: A review, Sci. Total Environ. 408 (2010) 3976–3989.
- [9] A. Wang, Q. Wu, C. Han, H. Yang, X. Xue, Significant influences of crystal structures on photocatalytic removal of NO_x by TiO₂, J. Photochem. Photobiol. A Chem. 407 (2021), 113020.
- [10] A.B. Oskooei, J. Koohsorkhi, M. Mehrpooya, Simulation of plasma-assisted catalytic reduction of NO_x, CO, and HC from diesel engine exhaust with COMSOL, Chem. Eng. Sci. 197 (2019) 135–149.
- [11] A.H. Mamaghani, F. Haghighat, C.-S. Lee, Photocatalytic oxidation technology for indoor environment air purification: The state-of-the-art, Appl. Catal. B 203 (2017) 247–269.
- [12] L. Zong, J. Zhang, G. Lu, Z. Tang, Controlled Synthesis of TiO₂ Shape and Effect on the Catalytic Performance for Selective Catalytic Reduction of NO_x with NH₃, Catal. Surv. Asia 22 (2) (2018) 105–117.
- [13] X. Wang, K. Maeda, A. Thomas, K. Takanabe, G. Xin, J.M. Carlsson, K. Domen, M. Antonietti, A metal-free polymeric photocatalyst for hydrogen production from water under visible light, Nat. Mater. 8 (1) (2009) 76–80.
- [14] S. Wang, C. Li, T. Wang, P. Zhang, A. Li, J. Gong, Controllable synthesis of nanotube-type graphitic C₃N₄ and their visible-light photocatalytic and fluorescent properties, J. Mater. Chem. A 2 (2014) 2885–2890.
- [15] M.A. Lafta, S.H. Ammar, H.J. Khadim, Z.H. Jabbar, Improved photocatalytic degradation of methyl violet dye and pathogenic bacteria using g-C₃N_A supported phosphotungstic acid heterojunction, J. Photochem. Photobiol. A Chem. 437 (2023), 114506.
- [16] M. Ismael, Facile synthesis of NiO-loaded g-C₃N₄ heterojunction photocatalyst for efficient photocatalytic degradation of 4-nitrophenol under visible light irradiation, J. Photochem. Photobiol. A Chem. 439 (2023), 114576.
- [17] J. Fu, J. Yu, C. Jiang, B. Cheng, g-C₃N₄-Based Heterostructured Photocatalysts, Adv. Energy Mater. 8 (3) (2018) 1701503.
- [18] W. Yu, J. Chen, T. Shang, L. Chen, L. Gu, T. Peng, Direct Z-scheme g-C₃N₄/WO₃ photocatalyst with atomically defined junction for H₂ production, Appl Catal B 219 (2017) 693–704.
- [19] A. Aghaei Sarvari, S. Zeinali Heris, M. Mohammadpourfard, S.B. Mousavi, P. Estellé, Numerical investigation of TiO₂ and MWCNTs turbine meter oil nanofluids: Flow and hydrodynamic properties, Fuel 320 (2022), 123943.
- [20] E. Sobhani, S.Z. Heris, S.B. Mousavi, The Synergistic Effect of Intumescent Fire-Resistive Paint Containing TiO₂ Nanoparticles and Chlorinated Paraffin onto Atmospheric-Metallic Substrates, ChemistrySelect 7 (2022) e202203513.
- [21] F. Yousefi, S.B. Mousavi, S.Z. Heris, S. Naghash-Hamed, UV-shielding properties of a cost-effective hybrid PMMA-based thin film coatings using TiO₂ and ZnO nanoparticles: a comprehensive evaluation, Sci. Rep. 13 (2023) 7116.
- [22] R. Javadpour, S.Z. Heris, Y. Mohammadfam, S.B. Mousavi, Optimizing the heat transfer characteristics of MWCNTs and TiO₂ water-based nanofluids through a novel designed pilot-scale setup, Sci. Rep. 12 (2022) 15154.
- [23] A. Al Mayyahi, B.M. Everhart, T.B. Shrestha, T.C. Back, P.B. Amama, Enhanced charge separation in TiO₂/nanocarbon hybrid photocatalysts through coupling with short carbon nanotubes, RSC Adv. 11 (2021) 11702–11713.
- [24] S.-H. Chiou, H.-C. Ho, H.-T. Liao, F.-Y. Tsai, C.-W. Tsao, Y.-J. Hsu, C.-H. Hsueh, Plasmonic gold nanoplates-decorated ZnO branched nanorods@TiO₂ nanorods

- heterostructure photoanode for efficient photoelectrochemical water splitting, J. Photochem. Photobiol. A Chem. 443 (2023), 114816.
- [25] A. Al Mayyahi, S. Sarker, B.M. Everhart, B. Tonyali, U. Yucel, P.B. Amama, Synthesis of ultrathin, nano-sized Ti₃C₂T_x with abundant =O and -OH terminals and high transparency as a cocatalyst: Enabling design of high-performance Titania-Ti₃C₂T_x hybrid photocatalysts, J. Phys. Chem. Solid 170 (2022), 110875.
- [26] J. Jia, Q. Zhang, K. Li, Y. Zhang, E. Liu, X. Li, Recent advances on g-C₃N₄-based Z-scheme photocatalysts: Structural design and photocatalytic applications, Int. J. Hydrogen Energy 48 (1) (2023) 196–231.
- [27] N.a. Tian, H. Huang, X. Du, F. Dong, Y. Zhang, Rational nanostructure design of graphitic carbon nitride for photocatalytic applications, J. Mater. Chem. A 7 (19) (2019) 11584–11612.
- [28] L. Lu, G. Wang, M. Zou, J. Wang, J. Li, Effects of calcining temperature on formation of hierarchical TiO₂/g-C₃N₄ hybrids as an effective Z-scheme heterojunction photocatalyst, Appl. Surf. Sci. 441 (2018) 1012–1023.
- [29] A. Kane, L. Chafiq, S. Dalhatou, P. Bonnet, M. Nasr, N. Gaillard, J.M.D. Dikdim, G. Monier, A.A. Assadi, H. Zeghioud, g-C₃N₄/TiO₂ S-scheme heterojunction photocatalyst with enhanced photocatalytic Carbamazepine degradation and mineralization, J. Photochem. Photobiol. A Chem. 430 (2022), 113971.
- [30] N.T. Thanh Truc, L. Giang Bach, N. Thi Hanh, T.-D. Pham, N. Thi Phuong Le Chi, D. T. Tran, M.V. Nguyen, V.N. Nguyen, The superior photocatalytic activity of Nb doped TiO₂/g-C₃N₄ direct Z-scheme system for efficient conversion of CO₂ into valuable fuels, J. Colloid Interface Sci. 540 (2019) 1–8.
- [31] L. Du, C. Jin, Y. Cheng, L. Xu, X. An, W. Shang, Y. Zhang, X. Rao, Improvement of antibacterial activity of hydrothermal treated TC4 substrate through an in-situ grown TiO₂/g-C₃N₄ Z-scheme heterojunction film, J. Alloy. Compd. 842 (2020), 155612.
- [32] M. Vijayan, V. Manikandan, C. Rajkumar, A.A. Hatamleh, B.K. Alnafisi, G. Easwaran, X. Liu, K. Sivakumar, H. Kim, Constructing Z-scheme g-C₃N₄/TiO₂ heterostructure for promoting degradation of the hazardous dye pollutants, Chemosphere 311 (2023), 136928.
- [33] J. Yu, S. Wang, J. Low, W. Xiao, Enhanced photocatalytic performance of direct Z-scheme g-C₃N₄-TiO₂ photocatalysts for the decomposition of formaldehyde in air, PCCP 15 (2013) 16883–16890.
- [34] A.A. Mayyahi, S. Sarker, B.M. Everhart, X. He, P.B. Amama, One-step fluorine-free synthesis of delaminated, OH-terminated Ti₃C₂: High photocatalytic NO_x storage selectivity enabled by coupling TiO₂ and Ti₃C₂-OH, Mater. Today Commun. 32 (2022). 103835.
- [35] Z. Wang, Y. Huang, M. Chen, X. Shi, Y. Zhang, J. Cao, W. Ho, S.C. Lee, Roles of N-Vacancies over Porous g-C₃N₄ Microtubes during Photocatalytic NO_x Removal, ACS Appl. Mater. Interfaces 11 (2019) 10651–10662.
- [36] I. Papailias, N. Todorova, T. Giannakopoulou, J. Yu, D. Dimotikali, C. Trapalis, Photocatalytic activity of modified g-C₃N₄/TiO₂ nanocomposites for NO_x removal, Catal. Today 280 (2017) 37–44.
- [37] X. Hu, Y. Wang, Z. Ling, H. Song, Y. Cai, Z. Li, D. Zu, C. Li, Ternary g-C₃N₄/TiO₂/Ti₃C₂ MXene S-scheme heterojunction photocatalysts for NO_x removal under visible light, Appl. Surf. Sci. 556 (2021), 149817.
- [38] X. Xie, N. Zhang, Positioning MXenes in the Photocatalysis Landscape: Competitiveness Challenges, and Future Perspectives, Adv. Funct. Mater. 30 (36) (2020) 2002528.
- [39] S. Devahasdin, C. Fan, K. Li, D.H. Chen, TiO₂ photocatalytic oxidation of nitric oxide: transient behavior and reaction kinetics, J. Photochem. Photobiol. A Chem. 156 (1-3) (2003) 161–170.
- [40] Q.L. Yu, H.J.H. Brouwers, Indoor air purification using heterogeneous photocatalytic oxidation. Part I: Experimental study, Appl. Catal. B: Environ. 92 (3-4) (2009) 454–461
- [41] B.M. Everhart, B. McAuley, A. Al Mayyahi, B. Tonyali, U. Yucel, P.B. Amama, Photocatalytic NO_x mitigation under relevant conditions using carbon nanotubemodified titania, Chem. Eng. J. 446 (2022), 136984.
- [42] M. Çağlayan, M. Irfan, K.E. Ercan, Y. Kocak, E. Ozensoy, Enhancement of photocatalytic NO_x abatement on titania via additional metal oxide NO_x-storage domains: Interplay between surface acidity, specific surface area, and humidity, Appl. Catal. B 263 (2020), 118227.
- [43] J. Wan, X. Du, R. Wang, E. Liu, J. Jia, X. Bai, X. Hu, J. Fan, Mesoporous nanoplate multi-directional assembled Bi₂WO₆ for high efficient photocatalytic oxidation of NO, Chemosphere 193 (2018) 737–744.
- [44] M.-H. Sun, S.-Z. Huang, L.-H. Chen, Y. Li, X.-Y. Yang, Z.-Y. Yuan, B.-L. Su, Applications of hierarchically structured porous materials from energy storage and conversion, catalysis, photocatalysis, adsorption, separation, and sensing to biomedicine, Chem. Soc. Rev. 45 (2016) 3479–3563.
- [45] P. Bairi, K. Minami, W. Nakanishi, J.P. Hill, K. Ariga, L.K. Shrestha, Hierarchically Structured Fullerene C70 Cube for Sensing Volatile Aromatic Solvent Vapors, ACS Nano 10 (2016) 6631–6637.
- [46] K.S.W. Sing, Reporting physisorption data for gas/solid systems with special reference to the determination of surface area and porosity (Recommendations 1984), 57 (1985) 603-619.
- [47] L. Wang, C. Xuan, X. Zhang, R. Sun, X. Cheng, Z. Wang, C. Ma, NO_x Adsorption Mechanism of Coal-Based Activated Carbon Modified with Trace Potassium: In Situ DRIFTS and DFT Study, Energy Fuels 36 (14) (2022) 7633–7650.
- [48] X. Zou, Y. Yang, H. Chen, X.-L. Shi, S. Song, Z.-G. Chen, Hierarchical meso/macro-porous TiO₂/graphitic carbon nitride nanofibers with enhanced hydrogen evolution, Mater. Des. 202 (2021), 109542.
- [49] J. Fang, H. Fan, M. Li, C. Long, Nitrogen self-doped graphitic carbon nitride as efficient visible light photocatalyst for hydrogen evolution, J. Mater. Chem. A 3 (26) (2015) 13819–13826.

- [50] A. Sekar, N. Metzger, S. Rajendran, A. Elangovan, Y. Cao, F. Peng, X. Li, J. Li, PtRu Catalysts on Nitrogen-Doped Carbon Nanotubes with Conformal Hydrogenated TiO₂ Shells for Methanol Oxidation, ACS Applied Nano Materials 5 (3) (2022) 3275–3288.
- [51] S. Abu Bakar, C. Ribeiro, An insight toward the photocatalytic activity of S doped 1-D TiO₂ nanorods prepared via novel route: As promising platform for environmental leap, J. Mol. Catal. A Chem. 412 (2016) 78–92.
- [52] H. Ma, Y. Li, S. Li, N. Liu, Novel PO codoped g-C₃N₄ with large specific surface area: Hydrothermal synthesis assisted by dissolution–precipitation process and their visible light activity under anoxic conditions, Appl. Surf. Sci. 357 (2015) 131–138.
- [53] H. Liu, D. Yu, T. Sun, H. Du, W. Jiang, Y. Muhammad, L. Huang, Fabrication of surface alkalinized g-C₃N₄ and TiO₂ composite for the synergistic adsorptionphotocatalytic degradation of methylene blue, Appl. Surf. Sci. 473 (2019) 855–863
- [54] Q. Wang, Z. Fang, X. Zhao, C. Dong, Y. Li, C. Guo, Q. Liu, F. Song, W. Zhang, Biotemplated g-C₃N₄/Au Periodic Hierarchical Structures for the Enhancement of Photocatalytic CO₂ Reduction with Localized Surface Plasmon Resonance, ACS Appl. Mater. Interfaces 13 (50) (2021) 59855–59866.
- [55] L. Lei, W. Wang, Y. Shang, J. Li, A. Kumar Yadav, H. Wang, Q. Li, H. Fan, Tailoring chemical structures and intermolecular interactions of melem intermediates for highly efficient photocatalytic hydrogen evolution of g-C₃N₄, Appl. Surf. Sci. 563 (2021), 150384.
- [56] J. Li, X. Liu, H. Che, C. Liu, C. Li, Facile construction of O-doped crystalline / non-crystalline g-C₃N₄ embedded nano-homojunction for efficiently photocatalytic H₂ evolution, Carbon 172 (2021) 602–612.
- [57] Y. Li, Y. Sun, W. Ho, Y. Zhang, H. Huang, Q. Cai, F. Dong, Highly enhanced visible-light photocatalytic NO_x purification and conversion pathway on self-structurally modified g-C₃N₄ nanosheets, Sci. Bull. 63 (10) (2018) 609–620.
- [58] R. Rajendran, S. Vignesh, A. Sasireka, S. Suganthi, V. Raj, P. Baskaran, M. Shkir, S. AlFaify, Designing Ag₂O modified g-C₃N₄/TiO₂ ternary nanocomposites for photocatalytic organic pollutants degradation performance under visible light: Synergistic mechanism insight, Colloids Surf A Physicochem Eng Asp 629 (2021), 127472.
- [59] S. Pahi, S. Sahu, S.K. Singh, A. Behera, R.K. Patel, Visible light active Zr- and N-doped TiO₂ coupled g-C₃N₄ heterojunction nanosheets as a photocatalyst for the degradation of bromoxynil and Rh B along with the H₂ evolution process, Nanoscale Adv. 3 (22) (2021) 6468–6481.
- [60] A.L.A. Parussulo, J.A. Bonacin, S.H. Toma, K. Araki, H.E. Toma, Unravelling the Chemical Morphology of a Mesoporous Titanium Dioxide Interface by Confocal Raman Microscopy: New Clues for Improving the Efficiency of Dye Solar Cells and Photocatalysts, Langmuir 25 (19) (2009) 11269–11271.
- [61] K. Maślana, R.J. Kaleńczuk, B. Zielińska, E. Mijowska, Synthesis and Characterization of Nitrogen-doped Carbon Nanotubes Derived from g-C₃N₄, Materials 13 (2020) 1349.
- [62] R.C. Pawar, S. Kang, S.H. Ahn, C.S. Lee, Gold nanoparticle modified graphitic carbon nitride/multi-walled carbon nanotube (g-C₃N₄/CNTs/Au) hybrid photocatalysts for effective water splitting and degradation, RSC Adv. 5 (31) (2015) 24281–24292.
- [63] H. Wang, X. Li, Q. Ruan, J. Tang, Ru and ${\rm RuO_X}$ decorated carbon nitride for efficient ammonia photosynthesis, Nanoscale 12 (23) (2020) 12329–12335.
- [64] Y. Zhang, Q. Pan, G. Chai, M. Liang, G. Dong, Q. Zhang, J. Qiu, Synthesis and luminescence mechanism of multicolor-emitting g-C₃N₄ nanopowders by low temperature thermal condensation of melamine, Sci. Rep. 3 (2013) 1943.
- [65] C.Y. Xu, P.X. Zhang, L. Yan, Blue shift of Raman peak from coated TiO₂ nanoparticles, J. Raman Spectrosc. 32 (2001) 862–865.
- [66] L.u. Yang, A. Hakki, F. Wang, D.E. Macphee, Different Roles of Water in Photocatalytic DeNO_x Mechanisms on TiO₂: Basis for Engineering Nitrate Selectivity? ACS Appl. Mater. Interfaces 9 (20) (2017) 17034–17041.
- [67] A.A. Mayyahi, S. Sarker, B.M. Everhart, X. He, P.B. Amama, One-Step Fluorine-Free Synthesis of Delaminated, OH-Terminated Ti₃C₂: High Photocatalytic NO_x Storage Selectivity Enabled by Coupling TiO₂ and Ti₃C₂-OH, Mater. Today Commun. 32 (2022), 103835.
- [68] C. Saka, Surface modification with oxygen doping of g-C₃N₄ nanoparticles by carbon vacancy for efficient dehydrogenation of sodium borohydride in methanol, Fuel 310 (2022), 122444.
- [69] A. Fujishima, X. Zhang, D.A. Tryk, TiO₂ photocatalysis and related surface phenomena, Surf. Sci. Rep. 63 (2008) 515–582.
- [70] O. Legrini, E. Oliveros, A.M. Braun, Photochemical processes for water treatment, Chem. Rev. 93 (2) (1993) 671–698.
- [71] J. Balbuena, G. Carraro, M. Cruz, A. Gasparotto, C. Maccato, A. Pastor, C. Sada, D. Barreca, L. Sánchez, Advances in photocatalytic NO_x abatement through the use of Fe₂O₃/TiO₂ nanocomposites, RSC Adv. 6 (78) (2016) 74878–74885.
- [72] M. Irfan, M. Sevim, Y. Koçak, M. Balci, Ö. Metin, E. Ozensoy, Enhanced photocatalytic NO_x oxidation and storage under visible-light irradiation by anchoring Fe₃O₄ nanoparticles on mesoporous graphitic carbon nitride (mpg-C₃N₄), Appl. Catal. B 249 (2019) 126–137.
- [73] A. Folli, J.Z. Bloh, K. Armstrong, E. Richards, D.M. Murphy, L.i. Lu, C.J. Kiely, D. J. Morgan, R.I. Smith, A.C. Mclaughlin, D.E. Macphee, Improving the Selectivity of Photocatalytic NO_x Abatement through Improved O₂ Reduction Pathways Using Ti_{0.999}W_{0.09102}N_x Semiconductor Nanoparticles: From Characterization to Photocatalytic Performance, ACS Catal. 8 (8) (2018) 6927–6938.